Romanian Reports in Physics **70**, 603 (2018)

ELECTRON DOSE DISTRIBUTIONS IN INHOMOGENEOUS PHANTOMS: A MONTE CARLO STUDY

D. MIHAILESCU, C. BORCIA

"Alexandru Ioan Cuza" University, Faculty of Physics, Carol I Blvd, No. 11, 700506, Iasi, Romania
E-mails: dmihail@uaic.ro; cborcia@uaic.ro

Received January 26, 2017

Abstract. Dose distributions in different models of inhomogeneous phantoms irradiated with 3–19 MeV electron beams have been calculated using DOSXYZnrc/EGSnrc Monte Carlo code. The rectilinear 3D voxel phantoms, relevant for radiotherapy and clinical dosimetry, were built from ICRU soft tissue equivalent material in which was inserted a single layer of bone, lung, air or Titanium. Significant interface effects have been found and qualitatively discussed.

Key words: relative dose distributions, transverse dose profiles, inhomogeneous phantoms, electron beams, IORT, Monte Carlo method, EGSnrc, BEAMnrc, DOSXYZnrc.

1. INTRODUCTION

In the human body there are, besides different soft tissues that are water equivalent and have similar radiological properties, inhomogeneities such as bones, lung or air cavities in which electron and photon radiation fields used in the external radiotherapy are strongly perturbed. Some patients can have metallic implants (prosthesis). These inhomogeneities significantly affect dose distributions in the irradiated volume and must be taken into account in the elaboration of the Treatment Plan [1, 2].

In order to achieve a uniform dose distribution inside the target volume and minimize the irradiation of the normal-tissue surrounding the target, ICRU Report 50 recommends an accuracy of 5% in dose delivery [3–5]. This requirement implies that a maximum 2%–3% uncertainty is allowed in the treatment planning calculations that is difficult to obtain in inhomogeneous tissues (see Table 1 from AAPM Report 85 [4]). Presently, dose calculation algorithms for Treatment Planning are classified into: (a) correction based algorithms (RTAR, ETAR) – fast but inaccurate near inhomogeneity (*i.e.* at interface), (b) model-based algorithms (Pencil-Beam Convolution/Superposition, Collapsed-Cone Convolution, Aniso-

tropic Analytical Algorithm) – fast enough, but inaccurate at interfaces, and (c) Monte Carlo-based algorithms: very accurate, but still time-consuming, not fully implemented, under development [7–10].

The Monte Carlo method is currently considered the most accurate method (the "golden standard") to simulate radiation beams produced by linear accelerators for radiotherapy and to calculate dose distributions in any geometry. Unlike all other methods that are basically analytical, even though some of them (like Superposition/Convolution method) use Monte Carlo pre-calculated dose kernels, Monte Carlo is a numerical "first principle" method in which the radiation transport is modelled using probability distributions. Unfortunately, the Monte Carlo method requires long execution times (large number of histories) to obtain small statistical errors. However, with the increasing of the computer speed combined with the decreasing hardware cost, one can expect that in the near future Monte Carlo based dose calculation algorithms will become available for routine clinical applications [10, 11].

In this context, the problem of inhomogeneities was and still is a relevant issue in radiotherapy and clinical dosimetry, reflected by the large number of papers published on this subject in the last few years [12–38]. Dose distributions of photons [12–28, 36, 37] and electron beams [29–35, 38] having different qualities have been investigated in various inhomogeneities with different degrees of complexity from simple planar layers of tissue equivalent materials (bone, lung) inserted at different depths in water, water equivalent or soft tissue equivalent materials (muscle, adipose tissue) [12–15, 18–20, 23–25, 28, 30, 33, 35, 37] to heterogeneities that mimic ribs, lung, skull [35] and ending with anthropomorphic phantoms [13, 30, 36]. Various air cavity geometries were also investigated [15, 17, 29, 31] because the perturbation caused by the air inhomogeneity near the tissue-air interfaces can be responsible for significant overdosing and underdosing of tumour or healthy tissues located in the vicinity of these interfaces. A particular case of inhomogeneities is represented by the metallic inserts such us Titanium used for some surgical implants [18, 22], dental prosthesis [16] or gold fiducial markers used in image-guided radiation therapy to correct for setup error and organ motion [21].

Analyzing the papers published in the last decades, some general ideas regarding dose distributions in inhomogeneous phantoms can be highlighted:

(i) The inhomogeneities were generally investigated in order to test or compare different classical algorithms [16–18, 22, 23, 25, 28, 29], to test general purpose Monte Carlo codes (such as EGS [15, 20, 21, 32, 37], GEANT4 [19], PENELOPE [24], MCNP4C [26]), or to validate commercially Monte Carlo Treatment Planning Systems [12–14, 23, 30, 33, 35]. The most accurate has been

found to be the Monte Carlo method; (ii) Irrespective of the type of radiation (electrons or photons), dose distributions (*i.e*. depth doses, beam profiles, isodose curves) are more or less affected by the presence of these inhomogeneities, depending by the beam quality (particle type, energy, angular and spatial distributions of the particles in the beam, beam size and incidence angle) and by inhomogeneity in the relation with the surrounding medium (location, size, mass and electronic density, effective atomic number), (iii) When a radiation beam passes from one medium to another having different scattering and absorption properties the shape of dose distributions may change dramatically, in some cases over 50% (see, for example, refs. [15] and [38]), (iv) A complete study of dose distributions should be performed inside, behind and, due to the interface effects, also in the front and on the lateral parts of the inhomogeneity, (v) The dose enhancements/reduction at interface is due to the backscattering processes which are well simulated by means of the Monte Carlo codes.

In this paper we focused on electron dose distributions in inhomogeneous phantoms made by single layers of bone, lung, air or Titanium sandwiched in tissue equivalent material.

The phantoms have been first irradiated with 3 and 7 MeV electron beams generated by NOVAC7, a linear accelerator for Intra-Operative Radiation Therapy (IORT) [39, 40]. To our knowledge, calculations of dose distributions in inhomogeneous phantoms for IORT electron beams have not yet been reported. The issue of inhomogeneities in the Intra-Operative Radiation Therapy has been only recently investigated, but exclusive for low-kV X-ray beams [41, 42].

In the case of NOVAC7 IORT accelerator, the maximum nominal energy is 9 MeV. In order to extent our work to higher energies, we also used mono-energetic 12 and 19 MeV electron beams. However, before entering the phantom, these beams cross a 1 cm thick layer of graphite that broads the energy and angular distributions of the electrons making them somewhat similar (but not identical) with those produced by a linear accelerator. These simulations have been performed for comparison purposes, having only a theoretical importance.

The IORT accelerator and the graphite slab were modelled using BEAMnrc/EGSnrc [43, 44] Monte Carlo code. For each simulated beam the complete information about any particle that crosses the scoring plane was stored in phase-space files used as inputs for DOSXYZnrc/EGSnrc Monte Carlo code [45, 46] to simulate electron dose distributions. The obtained results demonstrate that EGSnrc based Monte Carlo codes are appropriate tools to study the dose distributions and, even more important, the interface effects in inhomogeneous phantoms.

2. MATERIALS AND METHODS

2.1. MONTE CARLO SIMULATION OF THE ELECTRON BEAMS

IORT is a treatment modality of cancer which consists in the direct delivery of a high-level radiation dose (~ 20 Gy) to the residual tumour or to the tumour bed while the target area is exposed during surgery, after the removal of a neoplastic mass [39, 40, 47]. IORT is usually performed using 9–12 MeV electron beams produced by mobile *dedicated accelerators* directly co-located in the operating room. Presently there are three types of mobile linear accelerators for IORT: Mobetron [40], NOVAC7 [39, 47, 48] (and its new version NOVAC11 [49]), and LIAC [50, 51]. Mobetron is produced in the USA, NOVAC and LIAC in Italy.

In this work have been used radiation beams generated by NOVAC7. A Monte Carlo investigation of this IORT accelerator was earlier performed [48], its dosimetric characteristic being carefully determined. The NOVAC7 produces electron beams with four different energies (3, 5, 7 and 9 MeV) and is equipped with long PMMA cylindrical applicators with inner diameters 4, 6, 8 and 10 cm (resulting a number of 16 different beams). The source-to-surface distance (SSD) is 80 cm, except for the applicator with the diameter of 10 cm for which the SSD is 100 cm. Only two IORT beams (3 and 7 MeV) obtained with the reference applicator (10 cm diameter) were employed in this work.

The geometry of the NOVAC7® IORT accelerator (*i.e.* all of the essential components in the treatment head) was built using BEAMnrc/EGSnrc [43–45].

The accelerator was modelled as a series of simple BEAMnrc component modules with cylindrical symmetry centred on the *z*-axis (Fig. 1a). The complete information about the geometry and materials from the treatment head were provided by the manufacturer.

A number of 10^8 primary histories, *i.e.* initial electrons impinging on the exit window, were run for each nominal energy. A circular scoring plane (10 cm in diameter) was defined immediately after the IORT applicator (SSD = 100 cm).

The electron beam characteristics at the entrance of the treatment head (exit window) were determined by a tuning procedure described in detail in our previous works [48, 52], as a part of the commissioning process that involves comparison between the calculated and measured dose distributions in a water phantom (see the next paragraph).

In the BEAMnrc simulations both photons and electrons were transported down to 10 keV kinetic energies (ECUT = 0.521 MeV, PCUT = 0.01 MeV). The cross section data for all of the materials used in the simulations were obtained by the PEGS4 code [45] with AE = 0.521 MeV, AP = 0.01 MeV and density effect

corrections from the International Commission on Radiation Units and Measurements [53].

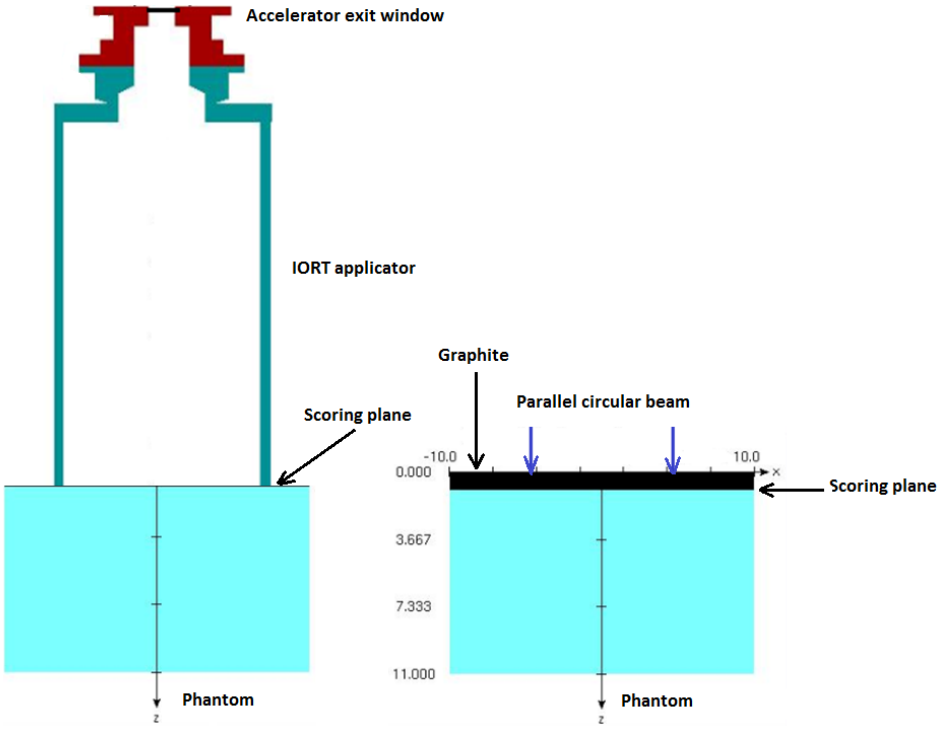

(a) (b)

Fig. 1 – 2D-models of the irradiation setups used in this work.
The homogeneous/ inhomogeneous phantoms have been irradiated with:
a) particle beams obtained using the NOVAC7 accelerator
(10 cm IORT applicator, 3 and 7 MeV nominal energies);
b) 12 and 19 MeV monoenergetic parallel circular beams (10 cm in diameter)
passing firstly through 1 cm of graphite (in black).

2.2. DOSE DISTRIBUTIONS IN HOMOGENEOUS PHANTOMS

The first dose calculations were done in homogeneous water and "soft tissue" virtual phantoms using DOSXYZnrc/EGSnrc Monte Carlo code [46]. The dose distributions in the water phantom were necessary to test the accuracy of the beam simulation. Then, the same electron beams were used in "soft tissue" phantoms to check the water-equivalency of this material.

We have modelled $20 \times 20 \times 5$ cm^3 and $20 \times 20 \times 10$ cm^3 rectilinear voxel phantoms, the deeper phantoms being used for higher nominal energies (12 and

19 MeV). For depth-dose calculations, the dose scoring grid was set to 1 cm × 1 cm × 0.1 cm (for 3 and 7 MeV) and 1 cm × 1 cm × 0.2 cm (for 12 and 19 MeV). For the transverse dose profiles the bin dimensions (cross-plane × in-plane × depth) of the dose computation grid were set to 0.5 cm × 0.5 cm × 0.4 cm (for all energies).

In DOSXYZnrc simulations the default values for EGSnrc particle's transport parameters have been used (PRESTA-I for boundary crossing algorithm and PRESTA–II as electron transport algorithm). The low energy thresholds for the production of knock-on electrons were set to AE = 0.521 MeV (total energy) and the threshold for bremsstrahlung events was set to AP = 0.010 MeV. The same values were also used for inhomogeneous phantoms. The number of histories was 4×10^7 for depth-dose curves and 10×10^7 for transverse dose profiles, which ensures a statistical uncertainty of about 0.2% (1 SD), excepting the depths beyond R_{50} for the depth dose distributions and the penumbra regions of dose profiles, where the statistical errors were several times larger. Because the number of particles in the BEAMnrc phase space files was usually lower than the necessary input, the recycle option have been used (*i.e.* the particles where reused two or three times, especially at low nominal energies when many initial electrons are absorbed in the accelerator head).

The 3 and 7 MeV IORT beams have been commissioned by comparing the experimental and Monte Carlo calculated dose distributions. Relative absorbed dose measurements were previously performed [48] by a PTW 23343 ion chamber and a PTW automatic water phantom with a spatial resolution of 0.5 mm.

After a number of simulations, an agreement of ±2% or ±1 mm between calculated and measured percentage depth doses (PDDs) was obtained, excepting some points at the phantom surface (Fig. 2a). Similar results were obtained for transverse dose profiles (TDPs) – see the reference [48]. This satisfactory agreement was achieved for an initial electron beam with 0.1 cm radius and 1° divergence at the exit vacuum window (point source).

The accuracy of our simulations was tested in water phantoms for 3 and 7 MeV IORT beams (Fig. 2a). However, for practical reasons (the human body is not entirely made by water), a tissue-equivalent material (ICRUTISSUE521ICRU) was used instead of water. This replacement will not change much the results because, this material is almost perfectly water-equivalent (Fig. 2b), especially at lower energies.

Two phantom materials are considered *exactly equivalent* if linear collision stopping power (S_{col}), linear radiative stopping power (S_{rad}) and linear scattering power (T) are identical for the whole electron range under consideration [5, 54–56].

Remember that the higher energies (12 and 19 MeV) are not actually IORT beams, but monoenergetic beams degraded through a graphite layer. A similar irradiation set up was used in reference [32] to study qualitative interface effects. As in our case, using this simple model meant that the photon and positron contamination from a realistic linac was not taken into account.

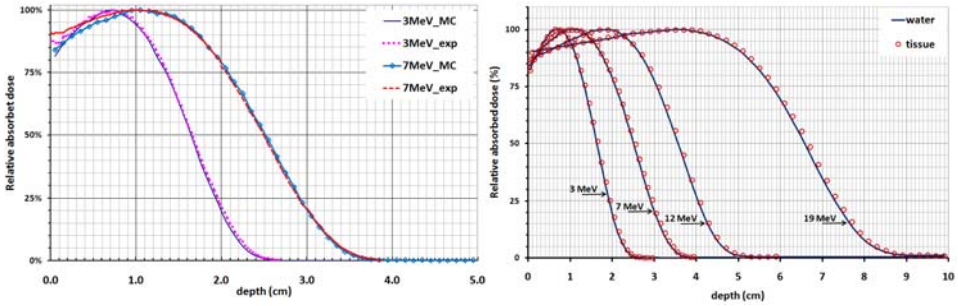

(a) (b)

Fig. 2 – a) Percentage dose distributions (PDDs) in a water phantom for 3 and 7 MeV beams generated by the NOVAC7 IORT accelerator (dashed lines – experimental values; solid lines – Monte Carlo values); b) percentage dose distributions (PDDs) calculated in water and soft tissue phantoms.

2.3. INHOMOGENEOUS PHANTOMS

Two types of inhomogeneous phantoms have been used in this work: phantoms with 1D-heterogeneities (Fig. 3), used for depth dose distributions and phantoms with 2D-heterogeneities (Fig. 4) involved in dose profiles calculation. The external dimensions and dose scoring grids of these phantoms are the same as those for the homogeneous phantoms described above. All phantoms are irradiated with normally incident circular radiation beams (10 cm in diameter).

All 1D-heterogeneities (bone, air, lung and Titanium) are sandwiched in tissue-equivalent material (ICRUTISSUE521ICRU) at a depth of 1 cm. In the first inhomogeneous phantom (Fig. 3a), the layer of bone-equivalent material (ICRPBONE521ICRU) has a thickness of 2 cm. In the second phantom (Fig. 3b), the layer of bone is replaced with a layer of air (AIR521ICRU) having the same thickness. The third phantom (Fig. 3c) contains 5 cm of lung-equivalent material (LUNG521ICRU). The Titanium (TI521ICRU) layer from the last 1D-phantom (Fig. 4d) has a thickness of 0.2 cm, this material having a much greater density than the others.

The material properties of all phantom materials are listed in Table 1. The relative numbers of elemental compositions and densities were considered by the PEGS4 data-preprocessing code [45] to create the data files containing information of material cross section and branching ratios.

The effective atomic numbers Z_{eff} were calculated according to ICRU Report 35 [2] as $Z_{eff} = \sum_t w_t Z_t^2 / \sum_t w_t Z_t$, where w_i and Z_i are the fractional weight and the atomic number of the *i-th* constituent of the material.

All 2D- heterogeneities are situated at the phantom surface and, excepting the Titanium inserts, have a thickness of 1 cm. 5 cm × 5 cm × 1 cm rectangular slabs made by (ICRPBONE521ICRU), air (AIR521ICRU) and lung

(LUNG521ICRU) are successively embedded in tissue-equivalent material (ICRUTISSUE521ICRU) (Fig. 4a).

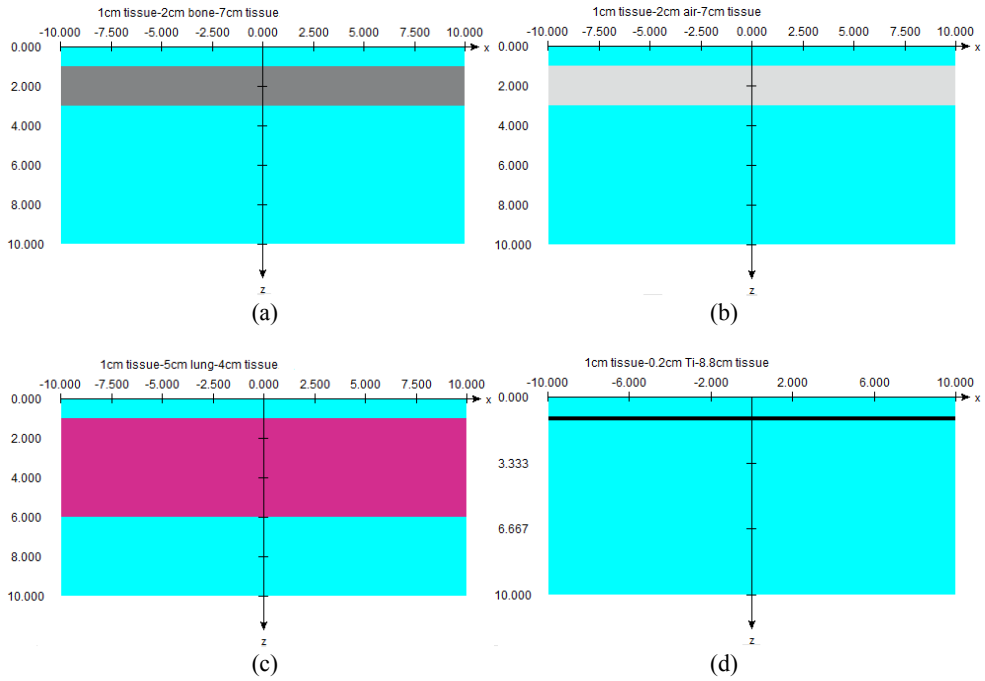

Fig. 3 – Phantoms with 1-D heterogeneity in the depth direction (scale drawing). Bone, air, lung, and Titanium layers are represented with different colours. Depth dose distributions were calculated along the central axis of the beam (the *z*-axis).

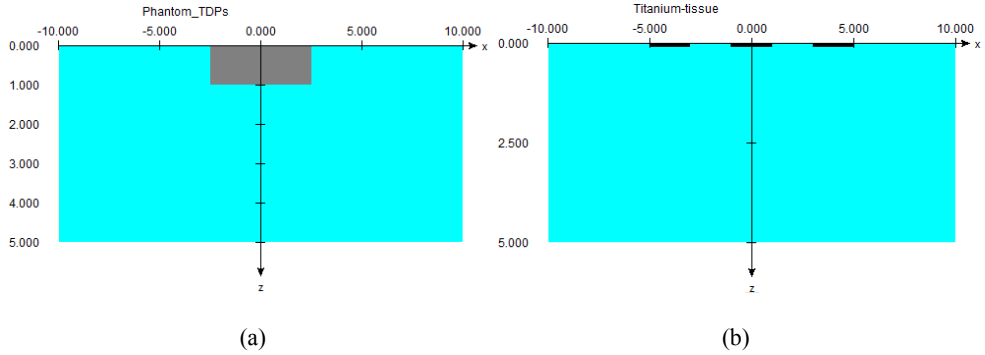

Fig. 4 – Phantoms with 2-D heterogeneity (scale drawing): a) bone, air, and lung slabs (in gray) have the same size and position. b) The Titanium slabs (in black) are described in the text. Transverse dose profiles were calculated along the *x*-axis immediately below heterogeneity (*i.e.*, at $z = 1.2$ cm for air and the "human tissues" and $z = 0.3$ cm for the Titanium implants).

Table 1

Elemental composition (fraction by weight), nominal density and effective atomic number of the materials used for the homogeneous and inhomogeneous phantoms studied in this work

	water	tissue	bone	air	lung	Ti
H (Z =1)	0.1119	0.1012	0.0472		0.1030	
C (Z = 6)		0.1110	0.1443	0.0001	0.1050	
N (Z = 7)		0.0260	0.0420	0.7553	0.0310	
O (Z = 8)	0.8881	0.7618	0.4461	0.2318	0.7490	
Na (Z = 11)					0.0020	
Mg (Z = 12)			0.0022			
P (Z = 15)			0.1050		0.0020	
S (Z = 16)			0.0032		0.0030	
Cl (Z = 17)					0.0030	
Ar (Z = 18)				0.0128		
K (Z = 19)					0.0020	
Ca (Z = 20)			0.2099			
Ti (Z = 22)						1.0000
Zn (Z = 30)			0.0001			
ρ [g/cm^3]	1.00	1.00	1.85	0.0012	0.26	4.54
Z_{eff}	7.22	7.68	13.61	7.60	7.91	22

In order to mimic the real implants, the Titanium slabs have a little more complex geometry. There are three identical smaller slabs (2 cm × 2 cm × 0.2 cm), equally distanced, the middle slab being centred on the *z*-axis (Fig. 4b).

3. RESULTS AND DISCUSSION

3.1. PHANTOMS WITH 1D-HETEROGENEITIES

The depth dose distributions calculated in phantoms with 1D-heterogeneities are shown in Figs. 5–8. For comparison, the dose values are expressed in Gy per particle. The term "particle" refers to the initially simulated particles (*i.e.* the primary electrons hitting accelerator exit window).

Before analysing in detail the behaviour of dose distributions, we should note that the inhomogeneity position relative to depth of maximum dose (z_{max}) in a homogeneous tissue phantom is different for the four nominal energies under consideration. The z_{max} values in homogeneous phantoms are 0.75 cm, 1.05 cm, 1.90 cm and 3.30 cm for 3 MeV, 7 MeV, 12 MeV and, respectively, 19 MeV.

In these conditions, the layers of bone/air/lung/Titanium are situated, in order, after z_{max}, near z_{max} and, for 12 and 19 MeV, beyond z_{max}.

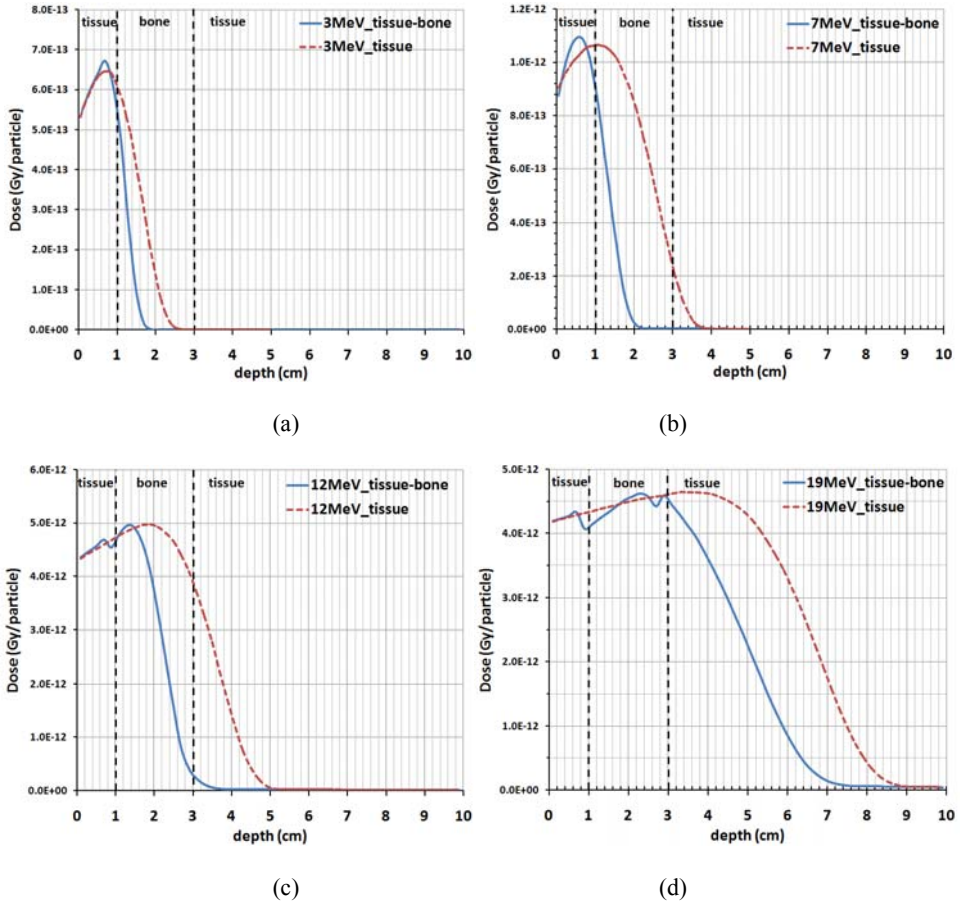

Fig. 5 – Depth dose distributions in tissue-bone-tissue phantom and homogeneous tissue phantom for: a) 3 MeV IORT beam; b) 7 MeV IORT beam; c) 12 MeV electron beam; d) 19 MeV electron beam.

3.1.1. Dose distributions inside and beyond the inhomogeneities

The behaviour of dose distributions inside the inhomogeneity is dictated mainly by the mass density of the material. Compared to soft tissue (or water), the beam attenuation is stronger for densities greater than 1 g/cm^3 and, contrarily, is weaker for lower densities. Therefore, the beams crossings low densities layers (such lung or air in our simulations) becomes more penetrating compared with the beams crossing homogeneous tissue phantom, affecting those tissues situated

beyond the inhomogeneitie (Figs. 6 and 7). High density layers (like bone and Titanium in our work) can significantly attenuate and even stop the radiation beam but, due to the backscattering process, may affect significantly the tissues located in the front of inhomogeneity (Figs. 5 and 8).

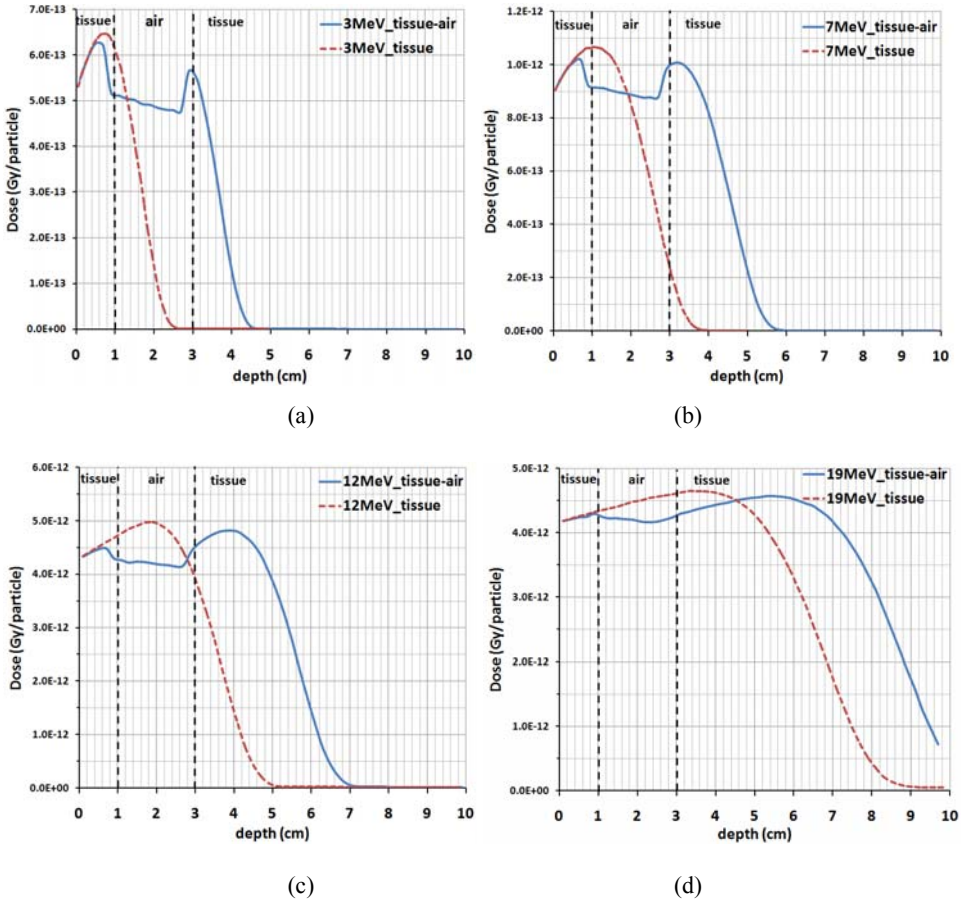

Fig. 6 – Depth dose distributions in tissue-air-tissue phantom and homogeneous tissue phantom for: a) 3 MeV IORT beam; b) 7 MeV IORT beam; c) 12 MeV electron beam; d) 19 MeV electron beam.

For inhomogeneous phantoms studied in this work, the dose values inside the inhomogeneity, excluding the narrow regions near the interface, are generally smaller than the corresponding values in the homogeneous tissue. It is the region in which dose calculation algorithms for Treatment Planning are accurate enough and we will not comment too much this issue. We note that the knowledge of dose values in bone and lung is mandatory in clinical dosimetry, whether or not they are

the target tissue. Doses inside air cavities and Titanium implants are irrelevant, particularly important being the interface effects, which will be discussed later.

As reported by ICRU 35 [2], dose distribution beyond the inhomogeneity can be corrected by using the coefficient of equivalent thickness (CET) method. For a parallel beam of incident radiation, CET is defined as the ratio of the thickness of water to that of the inhomogeneity that will produce the same transmission of absorbed dose rate. It is assumed that the attenuation by a given thickness t of the inhomogeneity is equivalent to the attenuation ($t \times$ CET) of water. The CET for a given material is approximately given by its electron density (electron/mL) relative to that of water, but can be roughly approximated with mass density [1, 2]. The dose at a point beyond the inhomogeneity is determined by calculating the effective depth, z_{eff}, along the ray joining the point and the virtual source of the electrons:

$$z_{eff} = z - t(1 - \text{CET}), \tag{1}$$

where z is the actual depth of the point of interest P from the surface. For CET < 1, $z_{eff} < z$, for CET > 1, $z_{eff} > z$.

In order to test the validity of the CET method, we have applied a scaling procedure in which the depth dose distributions for inhomogeneous phantoms were shifted towards z_{eff} calculated with the above formula and compared with dose distributions in homogeneous tissue phantoms. The curves for inhomogeneous phantoms containing air (CET ≈ 0) and lung (CET = 0.26) were moved toward the phantom surface with 2 cm (t_{air} = 2 cm; $z_{eff} - z = -2$ cm) and, respectively, 3.70 cm (t_{lung} = 5 cm; $z_{eff} - z = -3.70$ cm). On the contrary, the curves for phantoms embedding bone (CET = 1.85) and Titanium (CET = 4.54) had to be moved toward greater depths with 1.70 cm (t_{bone} = 2 cm, $z_{eff} - z$ = 1.70 cm) and, respectively, 0.71 cm (t_{Ti} = 0.2 cm; $z_{eff} - z$ = 0.71 cm). The CET method was considered valid if the dose distributions for homogeneous and inhomogeneous phantoms overlaps in a satisfactory way.

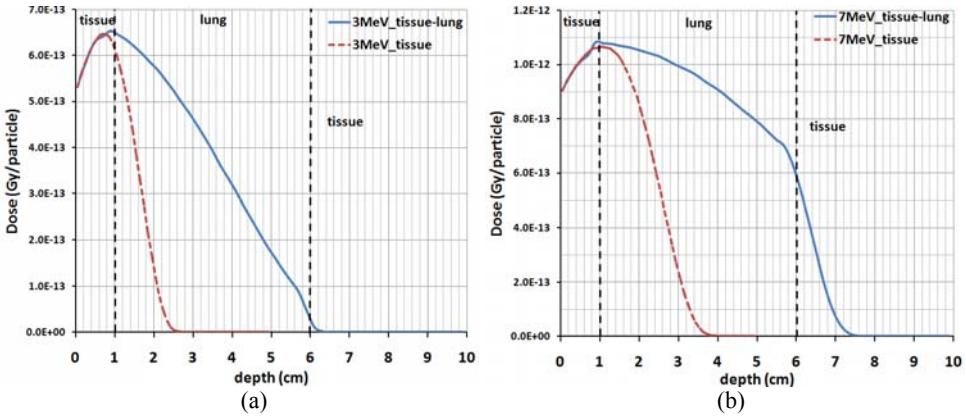

(a) (b)

Fig. 7

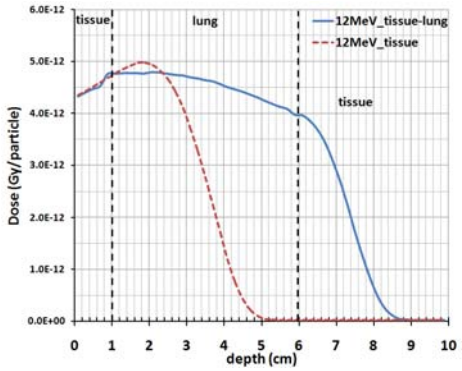

(c)

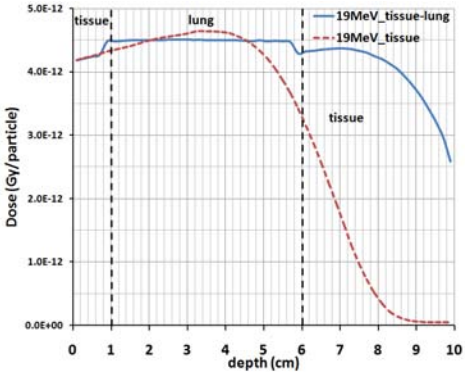

(d)

Fig. 7 (continued) – Depth dose distributions in tissue-lung-tissue phantom and homogeneous tissue phantom for: a) 3 MeV IORT beam; b) 7 MeV IORT beam; c) 12 MeV electron beam; d) 19 MeV electron beam.

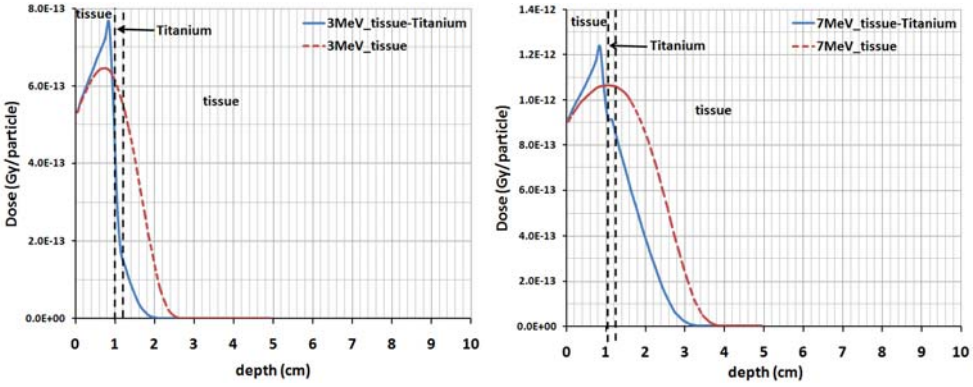

(a) (b)

Fig. 8

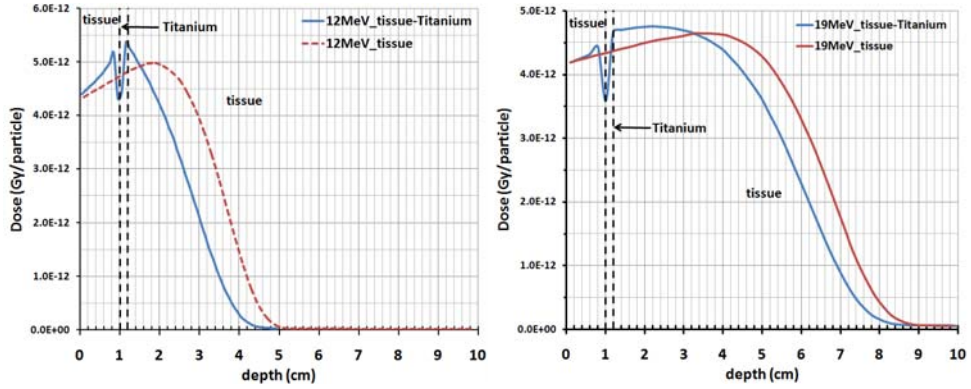

(c) (d)

Fig. 8 (continued) – Depth dose distributions in tissue-Ti-tissue phantom and homogeneous tissue phantom for: a) 3 MeV IORT beam; b) 7 MeV IORT beam; c) 12 MeV electron beam; d) 19 MeV electron beam.

For *tissue-air-tissue phantom*, good results were obtained for all beams (see, for example, Fig. 9b). For the other phantoms, only 19 MeV beams gave acceptable results (Fig. 9a, 9c and 9d). Not taking into consideration the interface effects, the difference between these results is due to the relationship between the attenuation/absorption and transmission.

The attenuation in air is almost negligible (Fig. 6), leaving practically unaffected the shape of the dose distributions beyond the inhomogeneity, regardless of the beam energy. The other materials, as we seen, have a different degree of attenuation. Thus, using density values from Table 1, it follows that a beam that would penetrate 1 cm of normal, unit density material (such as water or soft tissue), would penetrate about 3.85 cm depth in lung, 0.54 cm in bone, and 0.22 cm in Titanium. However, these values does not take into account the beam quality, the shape of dose distributions being very sensitive to the beam energy (Figs. 5 to 8).

In the case of *tissue-bone-tissue phantom*, the 3 MeV, 7 MeV and even 12 MeV electron beams, after crossing 1 cm of tissue, are completely or largely absorbed in the 2 cm layer of bone (Figs. 5a,b,c). Obviously, the CET method cannot be applied at these energies, but gives good results for 19 MeV beams (Fig. 9a).

In the case of lung *tissue-lung-tissue phantom*, the lower density is partially compensated by the greater thickness, such that the 3 and 7 MeV beams are strongly attenuated (Fig. 7a,b), somehow similarly with 2 cm of bone. The 12 MeV beam is partially transmitted (Fig. 7c), but insufficient to apply the CET method. Neither for the 19 MeV electron beam the results are not satisfactory, probably because the CET value (0.26) for lung is not suitable. As stated in reference [1],

there are experimentally evidences the CET values for lung depend on depth within the lung. In these conditions, some other empirical values for CET were proposed.

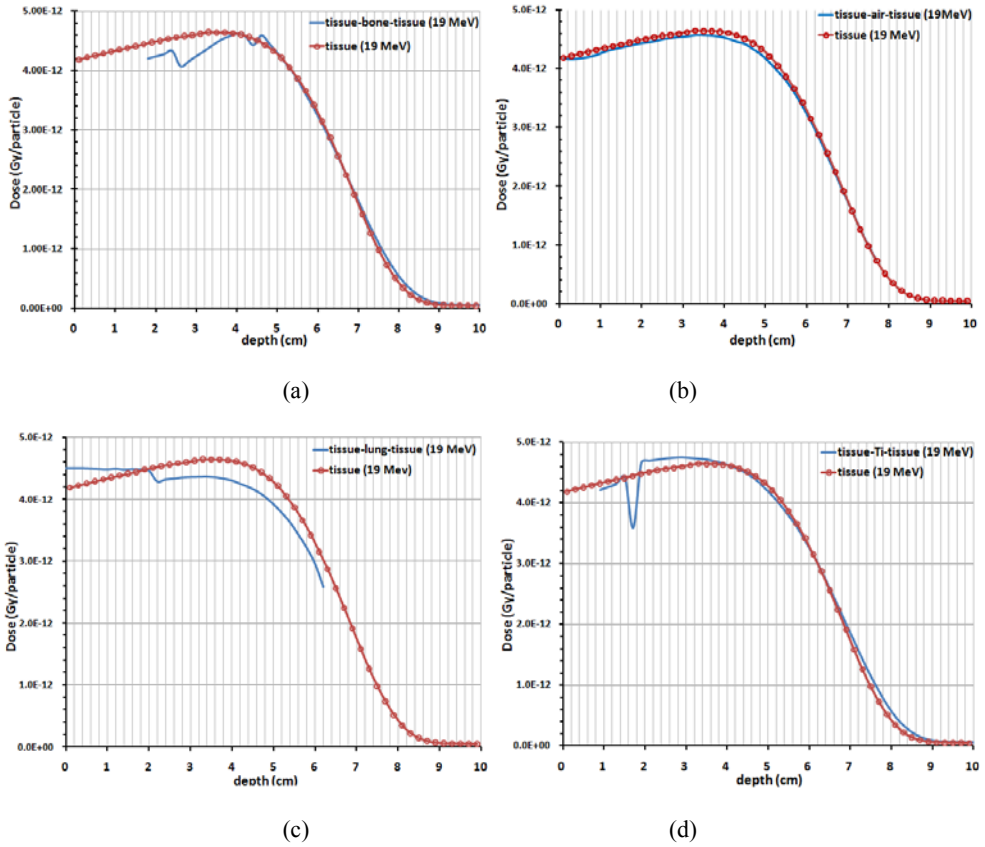

Fig. 9 – Illustration of the scaling method used to the test de validity of the CET method for the correction of dose distributions beyond the inhomogeneities. Depth dose distributions were shifted upstream (for inhomogeneous phantoms containing air and lung) and downstream (for inhomogeneous phantoms containing bone and Titanium).

A similar discussion can be done for the *tissue-Titanium-tissue phantom*. In our work, the greater density of the Titanium inhomogeneity is compensated by its decreased thickness (of only 0.2 cm). Also in this case, the results are becoming increasingly better as the energy beam is increased (Figs. 8 and 9d).

3.1.2. Dose distributions in the front of the inhomogeneities and interface effects

In this region, the dose distributions are strongly dependent on the density of the inhomogeneity but also on the beam energy, as we can see form the Figs. 5–8.

In order to simplify the discussion of the results, we will divide the inhomogeneities into two classes: high and low density inhomogeneities. The radiation beams will be also divided in low energy and high energy beams.

Low energy beams/high density inhomogeneities. For *low energy beams* (3 and 7 MeV) passing through phantoms containing *high density materials* (bone and Titanium), the doses in the front of the inhomogeneity increase significantly, due to the backscattered electrons. In the case of bone, the depth of maximum dose (z_{max}) is shifted toward the surface with 3 mm for the 3 MeV IORT beam (Fig. 5a) and 4 mm for the 7 MeV IORT beam (Fig. 5b), because of the greater energy of the backscattered electrons. A shifting of about 2 mm has been also obtained (Fig. 8a,b) in the case of Titanium layer for which, probably, the spatial resolution of 2 mm of our calculations is insufficient to highlight an energy dependence. These dose enhancements in the front of high Z heterogeneities is well documented and usually described by *Heterogeneity Correction Factors* (HCFs) defined as the dose at a point in a heterogeneous phantom (D_h) to that at the same point in a water phantom (D_w) – see, for example, the reference [13]. Similar correction factors can be calculated in our case using tissue instead of water. The percentage values for HCFs range between 1.04 (for bone/3MeV) and 1.19 (for Titanium/3 MeV). This means a significant overdosing (between 4% and 19%) of the tissue situated in the front of the inhomogeneity.

High energy beams/high density inhomogeneities. The overdosing effect of the high Z materials decrease with the increasing of the beam energy, because the fluence of the backscattered electrons decrease. Instead, depth dose distributions begin to exhibit a *dip and peak* behaviour near inhomogeneity, which is rather characteristic to dose profiles [32]. It is clear that this dose perturbation effects at both the entrance and exit interfaces between tissue and higher density inhomogeneities is due to an electronic disequilibrium, but the origin of this disequilibrium remain unknown without supplementary investigations of scattered electrons (fluence, angular and energy distributions). The enhancement and deficit of dose which can produce hot and, respectively, cold spots is more evident in the case of Titanium implants (*i.e.* it seems to be directly proportional to the material density). Regarding the energy dependence, the dose enhancements decrease with energy and the dose deficits increase with energy. Also, analyzing Fig. 5d, one can observe the contrasting behaviour of dose distributions at interfaces. At the entrance interface, the dose values first increase and then decrease. Contrary, at the exit interface, the dose values decrease and then increase. No dip and peak behaviour at the exit interface was observed in the case of Titanium layer, perhaps because of its small thickness.

Low density inhomogeneities. For *low and high energy beams* passing through phantoms containing *low density materials* (lung and air, in our case) the dose values in the front of inhomogeneity should decrease, due to the lack of the backscattering processes. This behaviour is much more evident in the case of air

for which the Heterogeneity Correction Factors (HCFs) have values smaller than unity but increasing with the beam energy to a value practical equal to unity. Dose values in the front of the lung layer is almost the same as the dose in the homogeneous tissue phantom, the interface effects being negligible.

3.2. PHANTOMS WITH 2D-HETEROGENEITIES

Transverse dose profiles (TDPs) calculated in phantoms with 2D-heterogeneities (bone, air and lung) are shown in Fig. 10 and for the phantom embedding Titanium layers in Fig. 11. The 2D-heterogeneities are located at the phantom surface (see Fig. 4 for the phantoms geometry). The TDPs have been calculated in the proximity of 2D-heterogeneities, at a depth of $z = (t_h + 0.2)$ cm (for inhomogeneous phantoms containing bone, air and lung) and $z = (t_{Ti} + 0.1)$ cm for the phantom embedding Titanium slabs. In the above formulas, $t_h = 1$ cm, $t_{Ti} = 0.2$ cm.

The results reveal strong perturbation of dose distributions, especially in the case of lower energy beams. In order to explain such perturbations, the TDPs from Fig. 10 were divided into different regions: (I) a central (*inner region*) between about –2.1 cm and + 2.1 cm, (II) two *edge regions* – few millimetres near the edge of the heterogeneities, situated at –2.5 cm and + 2.5 cm, on both sides, and (III) the *outer region*, the remaining dose distribution, including the penumbra region.

3.2.1. The inner region

Depending on the heterogeneity density, the transverse dose profiles should have in this region an opposite behaviour: the dose beyond low density materials (air and lung) should be higher and the doses beyond high density materials should be lower. This behaviour is respected only for 3 MeV IORT beam (Fig. 10a). For higher energies begin to emerge inversions, as we can see from Fig. 10b,c,d (for air and lung) and Fig. 10c,d for bone.

These inversions are due to the location of 2D-heterogeneities at the phantom surface, *i.e.* in the dose build-up region in which dose values increase from surface dose (D_s) toward the maximum dose (D_{max}). After D_{max}, the dose values decrease more or less steeply, depending on the material density and beam energy. Remember that the thickness of the heterogeneity is only 1 cm. After that, the beams passes through tissue and (as we already saw in the previous paragraph), significant interface effects can occur.

The behaviour of TDPs is ruled in the inner region by the relationship between depth of maximum dose (z_{max}) and the heterogeneity thickness as a function of the beam quality and material density. For the same energy, the dose increase is steeper and z_{max} is closer to the phantom surface for higher density materials. In effect, the build-up region is situated entirely inside the inhomogeneity in the case of bone (excepting the 19 MeV electron beam).

A different behaviour have lower density materials (lung and air). Thus, the maximum dose (D_{max}) is never reached in the lung slab (z_{max} ranges between 2.30 and 4.20 cm). The attenuation in 1 cm of air is negligible, this heterogeneity acting as a "missing tissue" (or "air gape").

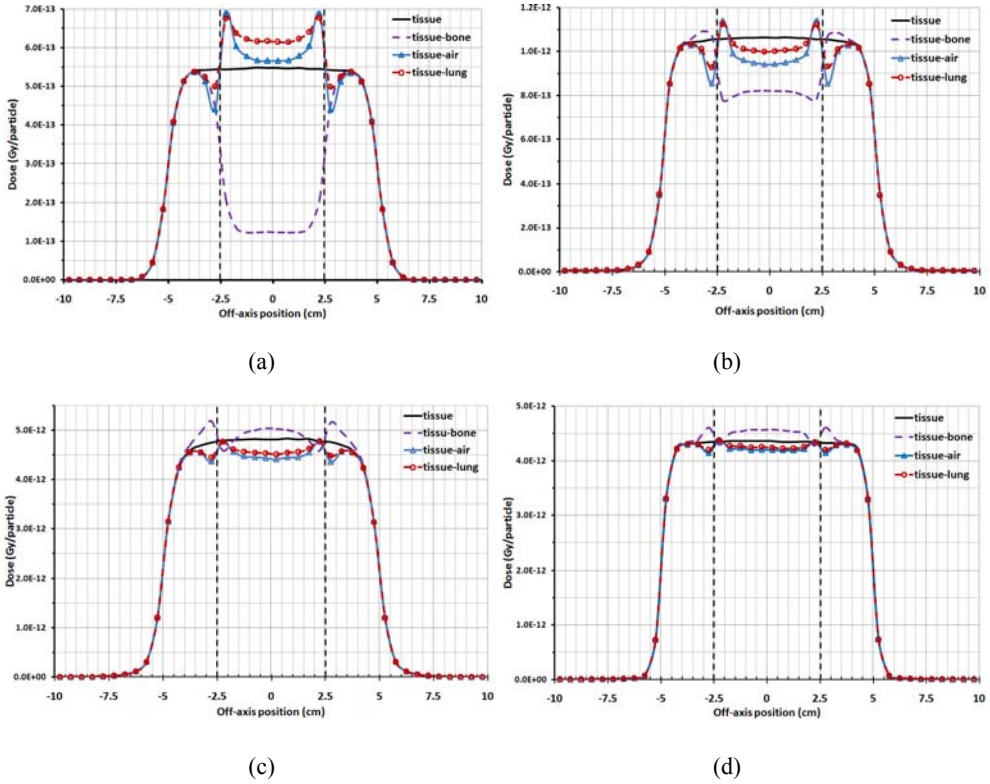

Fig. 10 – Transverse dose profiles calculated below 1 cm thick 2D-heterogeneities, at a depth z = 1.2 cm compared with dose profiles at the same depth in the homogeneous tissue phantom for: a) 3 MeV IORT beam; b) 7 MeV IORT beam; c) 12 MeV electron beam; d) 19 MeV electron beam.

To conclude, it is difficult to find a rule of thumb to describe dose distributions in this region, the dose values immediately beyond the heterogeneity relative to dose values in the homogeneous tissue being the result of dose build-up and build-down inside the heterogeneity and near the interface. Certainly, the CET method applied in the previous paragraph cannot be used so close to the interface where the Heterogeneity Correction Factors (HCFs) have so different values. For example, in the case of bone heterogeneity, HCF = 0.23, 0.77, 1.04, 1.05 for 3 MeV, 7 MeV, 12 MeV and, respectively, 19 MeV beam.

3.2.2. The edge regions

The main reason for choosing the study of dose distributions in phantoms containing 2D-heterogeneities was to investigate the edge effects.

The effects of electron scattering on the absorbed dose near the edge of an inhomogeneity is known for a long time. In an earlier paper, Shortt *el al*. [38] have investigated by the Monte Carlo method the interface effects induced by cylinders of air and aluminium embedded in a water phantom. The cylinders had 1 cm in diameter, a length of 2 cm (if air) or 1 cm (if aluminium) and were placed either 2 mm or 2 cm deep in the water phantom. Electron beams with the nominal energy of 10 MeV and 20 MeV have been used.

They found that effects of electron scattering on the absorbed dose are most dramatic near the edges of the inhomogeneities, where transverse dose profiles exhibited a "dip and peak" behaviour over the range of a few millimetres. Thus, beyond the aluminium cylinder whose density is greater than of its surrounding medium (water) they obtained an enhancement of the dose just outside its edge and a deficit in the dose just inside. This is because there are fewer electrons scattered in from the medium than scattered out from the high density inhomogeneity. This situation was reversed for air whose density is much less than that of water. Beyond the air, the dose is enhanced inside its edge and decreased outside because more electrons are scattered in from the medium that are scattered out by the inhomogeneity. These outcomes, obtained using EGS Monte Carlo code (version 4, available at that time) were satisfactory confirmed by the experiment.

We have obtained similar results for bone, air and lung slabs. Excepting the bone/3 MeV IORT beam, there are obvious dip and peaks characteristics just near the edges of these heterogeneities. For a given material, the dip and peaks magnitude is inversely proportional to energy, because the fluence of scattered electrons decrease with the energy. The dips and peaks are generally asymmetric, which it is difficult to explain without a quantitative analysis of the electron scattering processes.

3.2.3. The outer region

In this region, the dose distributions, especially in the penumbra region, are not affected by the presence of 2D-heterogeneities. It means that the edges of the heterogeneities are far enough away from the geometric beam edge. In other words, the range of the scattered electrons is insufficient to reach the penumbra region.

3.2.4. The Titanium implants

Similar considerations can be made to explain the Fig. 11 in which are shown the transverse dose profiles at a depth z = 0.3 cm, *i.e*. immediately behind the Titanium slabs. However, due to the particular choice of the slabs geometry (Fig. 4b), the dose distributions from Fig. 11 have different shape, compared with

those from Fig. 10. The main difference consists in the presence of dips and peaks in the central region, due to the edge effects.

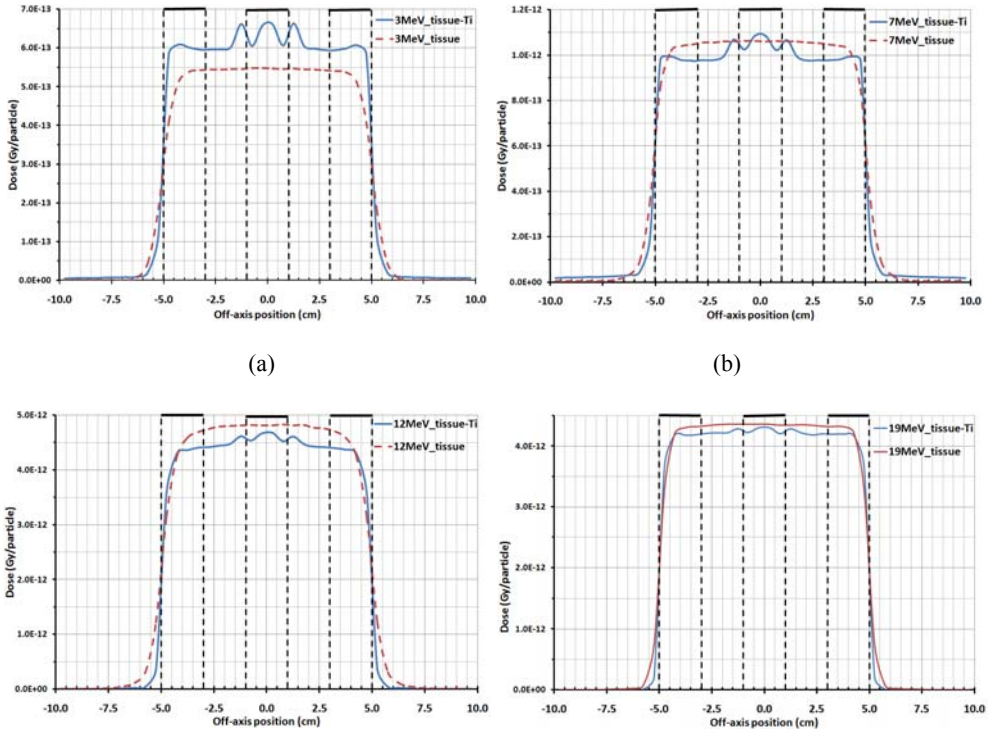

Fig. 11 – Transverse dose profiles calculated below 0.2 cm thick Titanium slabs, at a depth z = 0.3 cm compared with dose profiles at the same depth in the homogeneous tissue phantom.

4. CONCLUSIONS

Depth dose distributions and transverse dose profiles have been accurately calculated (0.2% statistical errors) in inhomogeneous tissue phantoms containing different 1D- and 2D- heterogeneities (bone, air, lung) and Titanium slabs (implants) for 3, 7, 12 and 19 MeV electron beams, using DOSXYZnrc/EGSnrc Monte Carlo code. The radiation beams were modelled with BEAMnrc/EGSnrc Monte Carlo code. The results have been compared with dose distributions calculated in homogeneous tissue phantoms. We found that the dose distributions are more or less affected by the presence of the inhomogeneities, depending by the beam energy and the type of the inhomogeneity. For completeness, the dose

perturbation effects have been analysed inside, beyond, in the front and on the lateral parts of the inhomogeneities (*i.e*. at the edges).

Significant dose perturbation effects have been found, especially at the interfaces, where the Heterogeneity Correction Factors may have appreciable values, leading to hot and cold spots (which should be taken into account in Treatment Planning). The dose perturbation effects are due: (i) to the electron scattering processes when the electron beam passes from one material to another with higher density; (ii) to lack of scattering when the electron beam passes from one material to another with lower density. In these two possible situations, the dose distributions have inversed behaviours. We also found that the dose perturbation effects are more significant at low energies and for inhomogeneities which have much different densities from those of the surrounding medium.

Our results demonstrate that the Monte Carlo method is an useful tool for the investigation of dose distributions in tissues with inhomogeneities.

REFERENCES

1. Faiz M. Kahn, John P. Gibbons, *The Physics of Radiation Therapy* (fifth edition), Chapter XIV (Electron Beam Therapy), Lippincott Williams & Wilkins, Philadelphia, 2014.
2. International Commission on Radiation Units and Measurements, *Radiation Dosimetry*: *Electron Beams with Energies between 1 and 50 MeV*, Report No. 35, Bethesda, MD: International Commission on Radiation Units and Measurements, 1984.
3. International Commission on Radiation Units and Measurements, *Prescribing, Recording, and Reporting Photon Beam Therapy*, Report No. 50, Washington, DC: International Commission on Radiation Units and Measurements, 1993.
4. N. Papanikolau, J. J. Batista, A. L. Boyer *et al.*, *Tisue Inhomogeneity Corrections for Megavoltage Photon Beams*, AAPM Report No. 85, AAPM TG65 (2004).
5. International Atomic Energy Agency (IAEA), *Absorbed Dose Determination in External Beam Radiotherapy: An International Code of Practice for Dosimetry Based on Standards of Absorbed Dose to Water* (Technical Report Series No. 398), IAEA, Vienna, 2000.
6. P. Almond, P. Biggs, B.M. Coursey *et al*., *AAPM's TG-51 protocol for clinical reference dosimetry of high-energy photon and electron beams*, Med. Phys. **26**, 1847–1870 (1999).
7. A. Ahnesjö and M. M. Aspradakis, *Dose calculations for external photon beams in radiotherapy*, Phys. Med. Biol. **44**, R99–R155 (1999).
8. T. Knoos, E. Wieslander, L. Cozzi *et al*., *Comparison of dose calculation algorithms for treatment planning in external photon beam therapy for clinical situations*, Phys. Med. Biol. **51**, 5785–5807 (2006).
9. I. Gagné and S. Zavgorodni, *Evaluation of the analytical anisotropic algorithm in an extreme water-lung interface phantom using Monte Carlo dose calculations*, J. Appl. Clin. Med Phys. **8** (1), 33–46 (2007).
10. N. Reynaert *et al*., *Monte Carlo treatment planning for photon and electron beams*, Radiat. Phys. Chem. **76**, 643–686 (2007).
11. I. J. Chetty, B. Curran, J. E. Cygler *et al.*, *Report of the AAPM Task Group No. 105: Issues Associated with Clinical Implementation of Monte Carlo-Based Photon and Electron External Beam Treatment Planning*, Med. Phys. **34** (12), 4818–4853 (2007).

12. C-M. Ma and J. Li, *Dose specification for radiation therapy: dose to water or dose to medium?*, Phys. Med. Biol. **56**, 3073–3089 (2011).
13. C-M. Ma, J. S. Li, T. Pawlicki, *et al*., *A Monte Carlo dose calculation tool for radiotherapy treatment planning*, Phys. Med. Biol. **47**, 1671–1689 (2002).
14. J. S. Li, T. Pawlicki, J. Deng, S. B. Jiang, E. Mok and C-M. Ma, *Validation of a Monte Carlo dose calculation tool for radiotherapy treatment planning*, Phys. Med. Biol. **45**, 2969–2985 (2000).
15. J. C. L. Chow and R. Jiang, *Bone and mucosal dosimetry in skin radiation therapy: a Monte Carlo study using kilovoltage photon and megavoltage electron beams*, Phys. Med. Biol. **57**, 3885–3899 (2012).
16. C. De Conto, R. Gschwind, E. Martin and L. Makovicka, *Study of dental prostheses influence in radiation therapy*, Physica Medica **30**, 117–121 (2014).
17. H. Jung, O. Kum, Y. Han *et al*., *Photon Beam Dosimetry with EBT3 Film in Heterogeneous Regions: Application to the Evaluation of Dose-calculation Algorithms*, Journal of the Korean Physical Society **65** (11), 1829–1838 (2014).
18. B. Brozyna, K. Chelminski, W. Bulski *et al*., *Dosimetry of dose distributions in radiotherapy of patients with surgical implants*, Radiat. Phys. Chem. **104**, 170–174 (2014).
19. C. I. Lee, J. W. Shin and S-C. Yoon, *Percentage depth dose distributions in inhomogeneous phantoms with lung and bone equivalent media for small fields of CyberKnife*, 2013 (http://arxiv.org/abs/1401.0692v1).
20. J. C. L. Chow and G. N. Grigorov, *Effect of the bone heterogeneity on the dose prescription in orthovoltage radiotherapy: A Monte Carlo study*, Reports of Practical Oncology and Radiotherapy **17**, 38–43, 2012 (available online at www.sciencedirect.com).
21. O. N. Vassiliev, R. J. Kudchadker, D. A. Kuban *et al.*, *Dosimetric impact of fiducial markers in patients undergoing photon beam radiation therapy*, Physica Medica **28**, 240–244 (2012).
22. J. T. Rakowski, K. Chin and S. Mittal, *Effects of titanium mesh implant on dosimetry during Gamma Knife radiosurgery*, J. Appl. Clin. Med Phys. **13** (5), 54–61 (2012).
23. A. Fogliata, G. Nicolini, A. Clivio, E. Vanetti and L. Cozzi, *Dosimetric evaluation of Acuros XB Advanced Dose Calculation algorithm in heterogeneous media*, Radiation Oncology, **6**, 82 (2011).
24. J. L. Vega Ramirez, F. Chen, P. Nicolucci and O. Baffa, *Dosimetry of small radiation field in inhomogeneous medium using alanine/EPR minidosimeters and PENELOPE Monte Carlo simulation*, Radiation Measurements **46**, 941–944 (2011).
25. L. A. R. da Rosa, S. C. Cardoso, L. T. Campos *et al.*, *Percentage depth dose evaluation in heterogeneous media using thermoluminescent dosimetry*, J. Appl. Clin. Med Phys. **11** (1), 117–127 (2010).
26. A. Alkhatib, Y. Watanabe and J. H. Broadhurst, *The local enhancement of radiation dose from photons of MeV energies obtained by introducing materials of high atomic number into the treatment region*, Med. Phys. **36** (8), 3543–3548 (2009).
27. M. Ravikumar, R. Ravichandran, S. Sathiyan, and S. S. Supe, *Backscattered Dose Perturbation Effects at Metallic Interfaces Irradiated by High-Energy X – and Gamma-Ray Therapeutic Beams*, Strahlentherapie und Onkologi **180** (3), 173–178 (2004).
28. J. C. L. Chow, R. Jiang and A. M. Owrangi, *Dosimetry of small bone joint calculated by the analytical anisotropic algorithm: a Monte Carlo evaluation using the EGSnrc*, J. Appl. Clin. Med Phys. **15** (1), 262–273 (2014).
29. M. Zarza-Moreno *et al.*, *Dosimetric effect by shallow air cavities in high energy electron beams*, Physica Medica (2013), http://dx.doi.org/10.1016/j.ejmp.2013.07.125.

30. J. F. Aubrya, H. Bouchard, I. Bessières, F. Lacroix, *Validation of an electron Monte Carlo dose calculation algorithm in the presence of heterogeneities using EGSnrc and radiochromic film measurements*, J. Appl. Clin. Med Phys. **12** (4), 2–14 (2011).
31. E. Chin, H. Palmans, D. Shipley, M. Bailey and F. Verhaegen, *Analysis of dose perturbation factors of a NACP-02 ionization chamber in clinical electron beams*, Phys. Med. Biol. **54**, 307–326 (2009).
32. F. Verhaegen, *Interface perturbation effects in high-energy electron beams*, Phys. Med. Biol. **48**, 687–705 (2003).
33. R. Doucet, M. Olivares, F. DeBlois *et al.*, *Comparison of measured and Monte Carlo calculated dose distributions in inhomogeneous phantoms in clinical electron beams*, Phys. Med. Biol. **48**, 2339–2354 (2003).
34. S. H. Cho and W. D. Reece, *Monte Carlo calculations of the dose backscatter factor for monoenergetic electrons*, Phys. Med. Biol. **44**, 13–26 (1999).
35. EuJin Chan, J. Lydon and T. Kron, *On the use of Gafchromic EBT3 films for validating a commercial electron Monte Carlo dose calculation algorithm*, Phys. Med. Biol. **60**, 2091–2102 (2015).
36. B. R. B. Walters, R. Kramer and I. Kawrakow, *Dose to medium* versus *dose to water as an estimator of dose to sensitive skeletal tissue*, Phys. Med. Biol. **55**, 4535–4546 (2010).
37. M. Miften, M. Wiesmeyer, A. Kapur and C.-M. C. Ma, *Comparison of RTP dose distributions in heterogeneous phantoms with the BEAM Monte Carlo simulation system*, J. Appl. Clin. Med. Phys. **2** (1), 21–31 (2001).
38. K. R. Shortt, C. K. Ross, A. F. Bielajew and D. W. O. Rogers, *Electron beam dose distributions near standard inhomogeneities*, Phys. Med. Biol. **1** (3), 235–249 (1986).
39. A. Rosi, V. Viti, *Rapporti ISTISAN* 03/ *Guidelines for quality assurance in intra-operative radiation therapy*, 2003.
40. A. Sam Beddar *et al.*, *Intra-operative radiation therapy using mobile electron linear accelerators:* Report of AAPM Radiation Therapy Committee Task Group No. 72, Med. Phys. **33**, *5*, 1476–1489 (2006).
41. A. Sethi, B. Chinsky, S. Gros, A. Diak, B. Emami, W. Small Jr, *Tissue inhomogeneity corrections in low-kV intra-operative radiotherapy (IORT)*, Transl. Cancer Res. **4** (2), 182–188 (2015).
42. S. Chiavassa, F. Buge, C. Herve, G. Delpon, J. Rigaud, A. Lisbona, S. Supiot, *Monte Carlo evaluation of the effect of inhomogeneities on dose calculation for low energy photons intra-operative radiation therapy in pelvic area*, Physica Medica **31**, 956–962 (2015).
43. D. W. O. Rogers, B. A. Faddegon, G. X. Ding, C-M Ma, J. We J and T.R. Mackie, *BEAM: a Monte Carlo code to simulate radiotherapy treatment units*, Med. Phys. **22**, 503–524 (1995).
44. D.W.O. Rogers, B. Walters and I. Kawrakow, *BEAMnrc Users Manual*, National Research Council of Canada, Report PIRS-0509 (A) revK, Ottawa, NRC (2007).
45. I. Kawrakow, E. Mainegra-Hing, D.W.O. Rogers, F. Tessier and B.R.B. Walters, *The EGSnrc Code System: Monte Carlo Simulation of Electron and Photon Transport*, NRCC Report PIRS-701, 2013 (http://irs.inms.nrc.ca/software/egsnrc/documentation.html).
46. B.R.B Walters, I. Kawrakow and D.W.O. Rogers, *DOSXYZnrc Users Manual*, NRCC Report PIRS-794revB (2006).
47. D. Mihailescu and C. Borcia, *Monte Carlo simulation of the electron beams produced by a linear accelerator for Intraoperative Radiation Therapy*, Rom. Rep. Phys. **66** (1), 61–74 (2014).
48. M. Pimpinella, D. Mihailescu, A. S. Guerra and R. F. Laitano, *Dosimetric characteristics of electron beams produced by a mobile accelerator for IORT*, Phys. Med. Biol. **52**, 6197–6214 (2007).

49. Sordina IORT Technologies spa (S.I.T.), *NOVAC11 Intra Operative Radiation Therapy dedicated mobile accelerator*, N300000-01-DPL Rev.B_EN October 2013 (http://soiort.com/wp-content/uploads/2013/12/Novac-11-Technical-Data.pdf).
50. G. Iaccarino, L. Strigari, M. D'Andrea *et al.*, *Monte Carlo simulation of electron beams generated by a 12 MeV dedicated mobile IORT accelerator*, Phys. Med. Biol. **56**, 4579–4596 (2011).
51. S. Righi, E. Karaj, G. Felici and F. Di Martino, *Dosimetric characteristics of electron beams produced by two mobile accelerators, Novac7 and Liac, for intraoperative radiation therapy through Monte Carlo simulation*, J. Appl. Clin. Med Phys. **14**, 6–18 (2014).
52. M. Oprea, C. Constantin, D. Mihailescu, C. Borcia, *A Monte Carlo investigation of the influence of initial electron beam characteristics on the absorbed dose distributions obtained with a 9MeV IORT accelerator*, U.P.B. Sci. Bull., Series A **74** (4), 153–166 (2012).
53. International Commission on Radiation Units and Measurements (ICRU), *Stopping Powers for Electrons and Positrons ICRU Report 37*, Bethesda, MD: ICRU, 1984.
54. D. Mihailescu, C. Borcia, *Water equivalency of some plastic materials used in electron dosimetry: a Monte Carlo investigation*, Rom. Rep. Phys. **58** (4), 415–425 (2006).
55. C. Borcia, D. Mihăilescu, *Are Water-Equivalent Materials Used in Electron Beams Dosimetry Really Water Equivalent?*, Rom. J. Phys. **53** (7–8), 851–863 (2008).
56. M. Oprea, D. Mihailescu, C. Borcia, *Monte Carlo evaluation of water equivalency of some plastic materials for realistic electron IORT beams*, Journal of Physics: Conference Series **398**, 012040 (2012).